Solar Spectroscopy

Dylan Nelson
University of California Berkeley
dnelson@berkeley.edu

December 8, 2006

Group Members - Trey Jalbert, Donald VanNess

Abstract

Using a table-top diffraction grating spectrometer, fiber fed through a local 8" telescope, we make spectroscopic observations scanning across the disk of the Sun. By taking sky spectra we can create a master sky spectrum of scattered light, and use it to correct for both dark current and sky contamination. Corrected solar spectra are smoothed and windowed, and then cross-correlated with a master reference spectra in order to determine the relative pixel shifts of solar absorption features occurring due to the Doppler shift of the rotating solar surface. Using high SNR we effectively measure the location of approximately 90 absorption lines in order to calculate relative shifts much smaller than the size of individual pixels on our CCD detector. We convert these shifts to units of wavelengths and use a theoretical solar disk crossing time 139.7 seconds to compute a solar rotation velocity of 1.576 ± 0.22 km/s. With a reference rotation period at the equator of 24.66 days, we estimate the radius of the Sun to be 534,600.0 $\pm$ 73,760.0 km.

1 Introduction

Measuring the physical radius of celestial objects, as opposed to their angular size on the sky, is one of the most basic problems in astronomy. The radius of the sun, for example, can be calculated without the need for any independent distance estimation. By observing the Doppler shift of electromagnetic waves free streaming from different locations on the solar surface we can use Equation 1 to calculate the surface rotational velocity.

$$v = \frac{\Delta\lambda}{\lambda}c \tag{1}$$

Here $\Delta\lambda$ is the wavelength shift from the rest wavelength λ, and c is the speed of light. With an independent measurement of the rotation period, say by observation of time-stable sunspots, the radius of a solid spherical body is given by:

$$R_\odot = \frac{v_{rot}T_{rot}}{2\pi} \tag{2}$$

Although the Sun is not a solid body and has a rotation rate dependent on latitude, we maintain this approximation by making observations at the equator. In what follows we attempt a measurement of v_{rot} with a reference period of solar rotation T_{rot} at the equator of 24.66 days.[1] In order to calculate the rotation speed, we develop a technique capable of differentiating shifts in spectral features smaller than the size of a single pixel, the basic resolving element of our spectrometer.

2 Equipment and Methods

Our solar spectrometer is a fiber-fed tabletop design, which removes the need for the apparatus to be directly mounted to the observing telescope. Light from an 8" Schmidt-Cassegrain telescope is projected onto a back plane with a fiber optic input centered in the middle. Light enters the fiber and is carried down to the spectrometer which can then be kept in a controlled and stable environment.

2.1 Spectrometer Setup

After exiting the fiber of diameter d_{fiber}, light radiation passes through a preliminary collimator, a narrow-band filter centered at 633 nm, and a primary collimator with focal length f_{coll}. Parallel light rays then diffract with incidence angle α and outgoing angle β from a blazed echelle grating with blaze angle δ and groove density σ. $2\theta = \alpha - \beta$ is the full angle between incident and diffracted rays, where by Equation 3:

$$\alpha = \delta + \theta, \beta = \delta - \theta \tag{3}$$

This diffracted beam then passes through a standard camera lens with focal length f_{cam} attached to the same Apogee AP47p CCD detector used previously. The Apogee has 1056 pixels along the dispersion direction, with a CCD pixel size of Δs. The nominal optical properties of our spectrometer are summarized in Table 1:

σ	80 mm^{-1}
δ	64.5°
d_{fiber}	100 μm
f_{coll}	180 mm
f_{cam}	200 mm
Δs	13 μm
2θ	10°

Table 1. Nominal spectrometer properties as described above. σ is the groove density, δ the blaze angle, d_{fiber} the fiber diameter. f_{coll} and f_{cam} are the collimator and camera focal lengths, respectively, and Δs is the size of a single CCD pixel. 2θ is the full angle between the incident and diffracted beams.

2.2 Spectrometer Characteristics

The primary relation from physical optics which governs the diffraction grating is the grating equation:[2]

$$m\frac{\lambda}{\sigma} = sin\,(\alpha) \pm sin\,(\beta) \tag{4}$$

Where α and β are given by Equation 3, m is the interference order, λ is the wavelength, and σ is the groove density. $+$ and $-$ correspond to reflection and transmission gratings, respectively. Several important characteristics of our spectrometer are briefly explored in order to better understand its operation. For a blazed diffraction grating, the order of diffraction is given[3] by Equation 5:

$$m = 2\frac{\sigma}{\lambda}sin\,(\delta)\,cos\,(\theta) \tag{5}$$

Where δ is the blaze angle. For our setup, we calculate a blaze order of 35.52. Roughly half

the light intensity is then split between orders 35 and 36. In order to perform calibration, detailed in Section 3, we align our CCD with the 35^{th} order for the remainder of this experiment. At $m = 35$, the free spectral range $\Delta\lambda = \lambda/m$. The minimum and maximum wavelengths of this order are then $\lambda_{mm} = \lambda \pm \Delta\lambda/2$. Differentiating Equation 4 with respect to β we can solve for the angular dispersion $\delta\beta/\delta\lambda$. Multiplying by the free spectral range yields the total angular spread of the order $\Delta\theta_m$:

$$\Delta\theta_m = \left(\frac{\delta\beta}{\delta\lambda}\right)\Delta\lambda = \frac{m}{cos\,(\beta)}\frac{\Delta\lambda}{\sigma} \tag{6}$$

The magnification of the system along the dispersion direction is given classically by

$$M_{\parallel} = \frac{f_{cam}}{f_{coll}} \tag{7}$$

On the other hand, light rays traveling orthogonal to the dispersion direction experience additional anamorphic magnification, resulting in a total magnification of

$$M_{\perp} = \frac{f_{cam}}{f_{coll}}\frac{cos\,(\alpha)}{cos\,(\beta)} \tag{8}$$

The size of a single spectral resolution element Δp (i.e., the image of the fiber on the CCD) can be approximated in terms of number of pixels covered as in Equation 9:

$$\Delta p = \frac{d_{fiber}M}{\Delta s} \tag{9}$$

Similarly, the spectral dispersion D of incoming light along the CCD pixels was determined analytically by matching up terms of units (nm/deg) and (deg/px), our conclusion being that

$$D = \frac{\Delta\lambda}{\delta\beta/\delta\lambda}\left(\frac{d_{pixel}}{f_{cam}}\right)^{-1} \tag{10}$$

Using this value we can quickly calculate the width of the order on the CCD in terms of both pixels and nm. In pixels, $\Delta m = D^{-1}\Delta\lambda$, which can be converted to units of wavelength by multiplying by Δs, the size of a single pixel.

2.3 Spectral Resolution

Finally, and of the greatest importance, we consider the resolution of the spectrometer. The spectral resolution R is defined as

$$R = \lambda/\delta\lambda. \tag{11}$$

For a diffraction grating spectrometer, the unitless resolution is given by:[4]

$$R = \frac{m\lambda}{\sigma}\frac{1}{cos\,(\gamma)\,cos\,(\alpha)}\frac{f_{coll}}{d_{fiber}} \tag{12}$$

Where γ is the angle of the incident beam above the plane formed by the dispersion direction of the grating, which in our case is assumed to be close to zero. The third term is a limiting factor imposed on the spectral resolution by the illumination source - the end of the fiber optic cable. That is, since the fiber is not a point source, information from a single wavelength is spread out over the size of the fiber on the CCD, resulting in a loss of resolution. This factor can be compared against the loss of resolution resulting from the diffraction limit.

The diffraction limited and slit limited resolution values, R_{DL} and R_{SL}, can be calculated separately and compared. Whichever is smaller represents the true limiting factor of the system. If the apparatus is "slit limited", decreasing the fiber diameter would allow resolution increases up to the diffraction limit, the tradeoff being a lower transmission efficiency in the fiber with decreasing cross-sectional area. In our case a rough calculation gave $R_{DL} \simeq 50\ R_{SL}$. As a result we are in the "slit limited" case, as opposed to the "diffraction limited" case.

All of the nominal characteristics of our spectrometer setup were calculated using the previously detailed method, and the results are given in Table 2, where the only unmentioned quantity is the spectral resolution in velocity units, which can be calculated as $R_{vel} = c/R$, where c is the speed of light.

2.4 Geometrical Considerations

Before conducting any observations of the Sun, we should consider how data must be collected in order to successfully make an estimate of its radius. Since the ecliptic of the Earth's motion is not in the plane of the Sun's equator, there is an angle of tilt φ of the Sun with respect to our observations. This angle is dependent on the day of the year, and can be retrieved from an online solar ephemeris[5], where it is given as the heliocentric latitude. This angle is zero when the Earth lies in the solar equatorial plane, which occurs during the Winter and Summer Solstice.

m_{calc}	35.52
m_{used}	35
$\Delta\lambda$	18.08 nm
λ_{min}	623.76 nm
λ_{max}	641.84 nm
$\Delta\theta_m$	0.0997°
$M_{\parallel}$	1.11
M_{ana}	0.69
$M_{\perp}$	0.77
$\Delta p_{\parallel}$	5.90 px
$\Delta p_{\perp}$	8.55 px
D	0.0118 nm/px
1/D	84.8 px/nm
R	9108
R_{vel}	32.9 km/s
Δm_{px}	19.93 mm
Δm_{λ}	1553.2 px

Table 2. Calculated spectrometer characteristics. Each value and its derivation are explained in detail in the previous discussion. We note only that Δm_{λ} is Δm_{px} in units of length instead of pixels.

The face-on tilt, or position angle θ, is also variable and can be retrieved from the same source. Figure 1 is a visualization of the spherical body of the sun at a position angle of 16.9° and heliocentric latitude of 1.2°, as on 29 November.

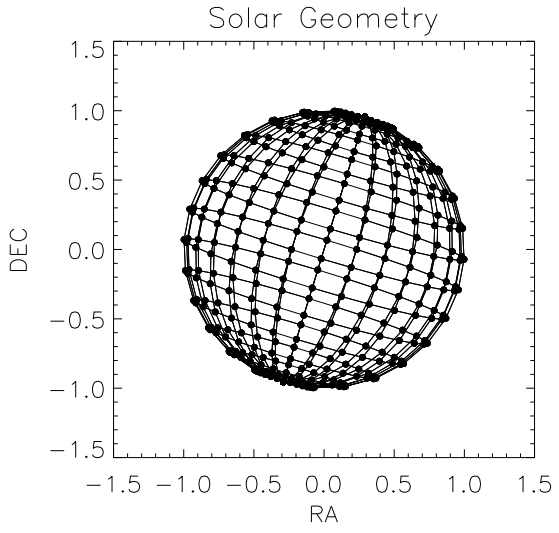

Figure 1. The sphere of the sun as seen by an observer on Earth on the 29^{th} of November, 2006. A position angle of 16.9° and a heliocentric latitude of 1.2° result in a tilted Sun with respect to the Earth. Lines of constant latitude and longitude are shown.

Finally, we let ψ be the angle from the equator of our observation (where $\psi = 90°$ represents the extreme limb of the Sun). If we measure an observed velocity of v_{obs}, its relation to the true rotational velocity v_{rot} is then given by the expression in Equation 13:

$$v_{obs} = v_{rot} cos\,(\varphi)\, cos\,(\theta)\, sin\,(\psi) \qquad (13)$$

As a result, we could attempt to take data at an angle from the apparent equator equal to the heliocentric latitude in order to scan across the true equator. In our particular case, however, this angle is negligibly small. The use of this correction factor is further discussed in Section 5 when we use it to calculate the true rotation velocity of the Sun.

3 Neon Calibration

Due to the extreme difficulty in analytically calculating where a given wavelength will fall on the CCD, we instead use a neon calibration source. Substituting the neon light source for our solar fiber source, we can observe distinct emission lines at certain locations on the CCD. By using their known laboratory wavelengths[6], as given in the NIST Handbook of Basic Atomic Spectra, we can calculate a calibration solution for use with later solar observations.

A series of 30 spectra were taken of the neon source, each with an exposure time of 1.5 seconds. This gave a high data number count in the brightest emission areas, though it did not saturate the detector. All 30 spectra were composited together with a simple sum in order to increase signal to noise. This master neon spectra is displayed in its original two-dimensional form in Figure 2:

We immediately notice four prominent neon emission lines. However, a line drawn through them does not run parallel to the x-axis. This is indicative of an axis of increasing wavelength not coinciding with the increasing x direction of the CCD chip. In order words, lines of constant wavelength were inclined with respect to the y-axis. In order to correct for this rotation we iteratively fit 2D Gaussians to each of the emission lines in order to calculate their X and Y centers. We calculated a slope through these fit points of -0.00552 ± 0.000032, as shown in Figure 3.

By simple geometry the needed angle of rotation is then the arc-tangent of the slope. We cal-

Figure 2. Image of the master neon spectra, scaled between 40,000 and 50,000 ADUs for high contrast around the background level to highlight non-circular represents of the fiber on the CCD. The last emission feature appears strongly deformed from unknown reasons.

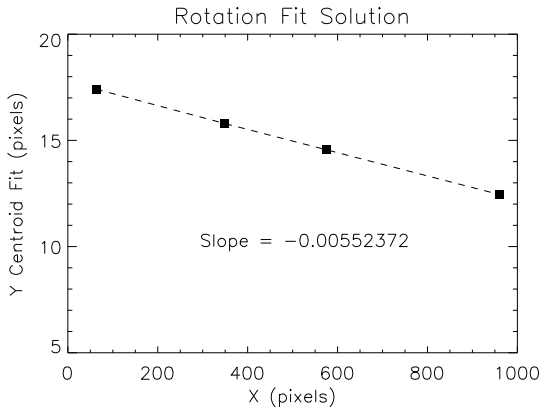

Figure 3. The y-coordinates of the neon emission lines plotted as a function of pixel distance along the spectrum. The slope indicates that the the axis of increasing wavelength is inclined with respect to the x-axis, where the angle of inclination is given by the arc-tangent of the slope of the best fit line.

Line	X (pixels)	λ (nm)	Strength
(1)	62.9747	626.6495	100P
(2)	349.018	630.4789	10
(3)	575.992	633.4428	100
(4)	960.220	638.2428	100P

Table 3. The four observed neon emission features and their corresponding laboratory rest wavelengths. The strengths of the lines are relative, with no absolute units. The P, where present, denotes a persistent line as described in the NIST Atomic Handbook reference.

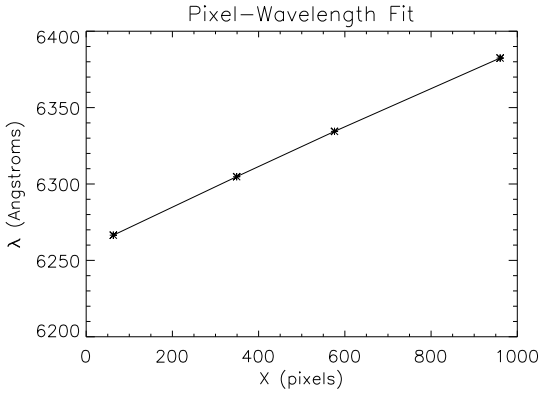

Figure 4. The rest laboratory wavelengths of the four neon emission lines as a function of the positions of the observed emission features. The linear fit is overplotted as a solid line. This calibration solution allows calculation of the observed wavelength corresponding to any pixel position along the spectrometer.

culated an optimal rotation of $-0.316°$, and rotated the master neon spectra using the `ROT` procedure and a cubic convolution interpolation routine to allow for rotation of a rectilinearly gridded array through any arbitrary amount. After this rotation we re-calculate the centroids of the four prominent emission features. By visual comparison with reference neon spectra from NOAO[7] we determined which emission lines our observed features correspond to. The x-coordinates and actual wavelengths are given in Table 3:

In order to compute a calibration solution we use the IDL procedure `SVDFIT` to perform a singular-value decomposition best linear fit. The resultant solution allows the computation of the wavelength corresponding to any given pixel position, to resolution even less than integer pixel steps. The fit is shown in Figure 4:

We calculated a slope of 0.129 ± 0.002 Angstroms/pixel, and a y-intercept of 6259.15 ± 0.95 Angstroms. Visually the calibration solution fit appears perfect. However, in order to get a clearer picture of the errors involved, we plot the residuals of the fit minus the data in Figure 5:

Upon closer inspection our fit does appear quite accurate, with deviation between theory and observation of less than 1 Angstrom in all cases. The residuals appear to follow a parabolic

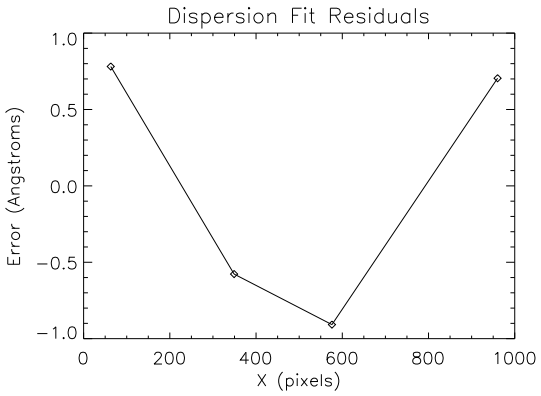

Figure 5. The residuals of the dispersion calibration fit. Calculated as the fit expectation value minus the actual data at that point, plotted at the four emission features. We observe an error which is in all cases less than one Angstrom. Additionally, the residuals appear to follow a quasi-parabolic pattern.

parent function, with positive error on the physical extremes of the CCD chip and negative error in the center of the chip. This is undoubtedly a result of the diffraction of the light beam from the echelle grating. Due to path length differences, the optimal CCD surface would actually be parabolic. Instead, we incur the error of a parabolic projection on a planar surface. This could be accounted for during data reduction by utilizing a more sophisticated fitting mechanism. However, the increased precision was not expected to be significant, especially when our focus is only on relative, and never absolute, wavelength shifts.

With our calibration fit we can estimate the spectral resolution of the spectrometer in units of distance along the CCD as well as in units of velocity. A Gaussian profile fit to the most prominent emission line yields a FWHM of 4.21 pixels, corresponding to 0.054 nm. Using Equation 1 we calculate an equivalent spectrometer resolution of 25.78 ± 0.03 km/s.

4 Solar Observations

With our calibration solution in hand we proceeded to make several observations of the Sun. Data was collected on November 27, 28, and 29. Each day involved slight modifications to the procedure, including the readout size from the CCD and the exposure times used. Some days also had tracking errors and/or cloudy weather conditions making observations suspect. On 29 November six data sets were taken, two across the apparent equator, and four more at varying angles from the midpoint of the solar disk. In each case the telescope was pointed to the declination of the Sun and slewed in right ascension. The tracking motor was disabled, such that the Sun naturally crossed through the field of view of the telescope along its ecliptic due to the rotation of the Earth. Continuous exposures were taken by the CCD camera through this timeframe. The mean of the resultant images is plotted as a function of time, extracted from the FITS header, in Figure 6:

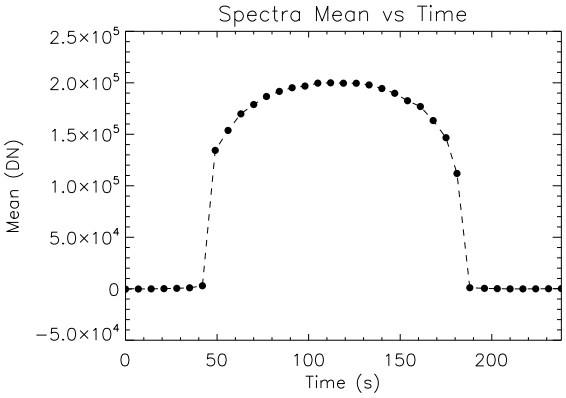

Figure 6. Mean value of individual solar spectra as a function of observed time. The flat segments represent exposures over background sky, recording contributions from scattered light only. Those with much higher means represent exposures taken with the fiber tracking over the surface of the sun.

Images in the beginning and end of the observation were subsequently used in order to create a master sky frame for sky subtraction. Those in the center, representing exposures with the fiber measuring direct Sun light, were used for rotational velocity measurements.

5 Data Reduction

For the 29 November data the first six exposures were combined with the final seven to construct a master sky frame. This frame was created as a median through the cube of 2D spectra images prior to changing them into one-dimensional spectra. This master sky frame was then subtracted pixel by pixel from every science frame. With this operation we effectively account for the dark current of the CCD for our given exposure time, as well as the removal of the con-

tribution from scattered light contaminating our solar spectra.

After sky subtraction the sun spectra images were rotated with the correction angle as described in Section 3. The 2D images were then totaled by column, with a column height of 12 pixels. This height contains effectively all of the information about the solar spectrum, and prevents the inclusion of excess pixels which only introduce unwanted noise. We are then left with a series of one-dimensional spectra, each taken at varying distances from the center of the solar disk. Figure 7 shows the spectra of our centermost exposure, where the rotation velocity on the solar surface should be nearly perpendicular to our line of sight.

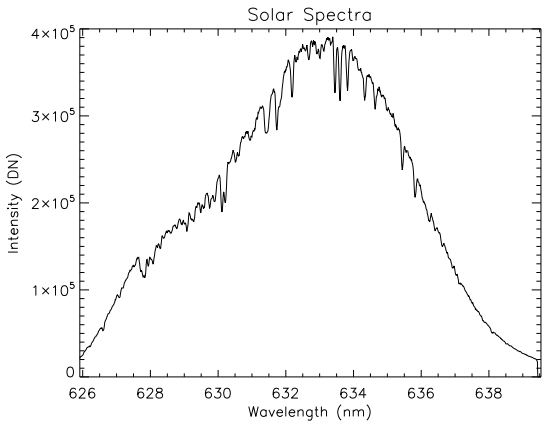

Figure 7. A single solar spectrum corresponding to exposure 16 of 35 from November 29. The raw 2D spectra image was sky-subtracted, rotated, and totaled along the y-axis. Theoretically, absorption lines in this spectra should exhibit zero Doppler shift, as all of the Sun's surface rotation is perpendicular to the observer's line of sight at the center of the solar disk.

The large scale structure evident in Figure 7 is a per-pixel sensitivity variation effect arising from the CCD as opposed to actual structure in the solar spectrum. We calculated the theoretical Planck blackbody function over the same wavelength range and observed a highly linear progression with a slight negative slope, since our narrow-band filter is towards the tail end of the blackbody spectrum. Flatfielding was attempting by using a "pure" white light source, however the improvement was minimal. Instead, we opted to simply remove the large scale structure to make the overall trend match the Planck function.

Two options were considered. First, the fourier transform of the individual spectra was taken, and the low frequency components excised in fourier space. The inverse fourier transform returns our original spectra with only the high frequency features (i.e., small absorption lines) intact. Alternatively, a simple running average was taken by convolving the spectra with a window of height unity and width approximately 60 pixels. The return is the large-scale structure, without any of the small features. For the November 29 data we used this second technique, subtracting this smoothed spectra from our original spectra. Figure 8 gives the smooth subtracted version of the above spectra.

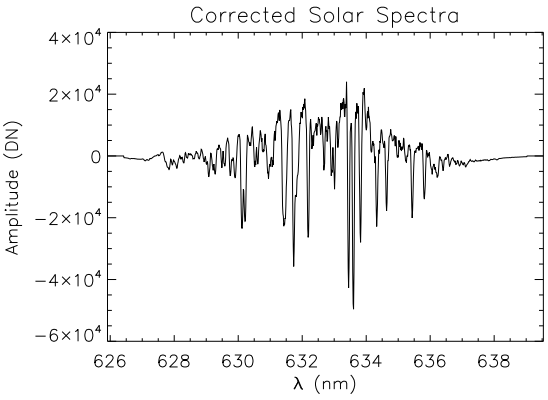

Figure 8. The same solar spectrum as above, with the large scale structure subtracted off. What remains is ideally a constant level of emission with well defined absorption features. A Hanning windowing function has also been applied to this spectrum, in order to make the function well behaved under a fourier transform.

In order to perform the fourier transforms on our spectra, we also implement a windowing function to enforce continuity at the x=0 and x=1056 pixel boundaries and eliminate spectral leakage. A simple Hanning windowing function is used, as the benefits of a more advanced windowing function are negligible in this case.[8] Figure 8 also includes the effect of multiplication by the Hanning window, which rises smoothly from zero to one and back to zero at the boundaries.

Visual observation reveals that the pixel shifts of absorption features in our spectra are extremely small, well shy of full integer pixel values. By substituting the definition of our spectrometer resolution (Equation 11) into the Doppler shift expression (Equation 1) we obtain $\Delta v = c/R$ for the achievable velocity resolution. How-

ever, if we consider the statistical significance of a high signal-to-noise ratio when determining the location of individual absorption lines, as well as the number of total lines we are able to measure, our velocity resolution becomes:[9]

$$\Delta v = \frac{c}{R} \simeq \frac{1}{SNR}\frac{1}{\sqrt{N}}\frac{c}{R}. \qquad (14)$$

Here N is the total number of lines measured, and $1/\sqrt{N}$ term is the standard decrease in error resulting from N independent measurements. To take advantage of the numerous absorption features present in our spectra, without individually calculating their positions, we perform a cross-correlation between each solar spectrum and the reference solar spectrum. Let s_i denote the ith spectra, and r the reference spectra, then the correlation of s_i and r is given by[10] Equation 15:

$$s_i * r = \int_{-\infty}^{\infty} s_i\,(\tau + t)\,r(t)d\tau \qquad (15)$$

Where the correlation is a function of the lag t. Equivalently, the Correlation Theorem allows us to express the correlation of s_i and r in terms of their fourier transforms, S_i and R:

$$s_i * r = S_i(f)R^{\star}(f) \qquad (16)$$

Where $R^{\star}$ represents the complex conjugation of R. We use Equation 16 to calculate the cross-correlations between all the solar spectra and the reference spectra. The maximum of the resulting correlation matrix is found, and a Gaussian profile is fit to the vicinity. The resultant fit is shown in Figure 9:

Once again we can verify the accuracy of the theoretical fit by calculating the residuals between the fit and the data. Since the absorption features are predominantly widened from the effects of the rotational Doppler shift, they assume a highly gaussian shape. Since the fourier transform of a gaussian is again a gaussian, the correlation between two spectra containing a large number of small gaussian features leads to a gaussian profile centered around the point of highest correlation. The residuals are extremely small, of order 0.1% of the peak intensity, and so the fit gives an x-coordinate centroid position which is accurate to a fraction of a pixel.

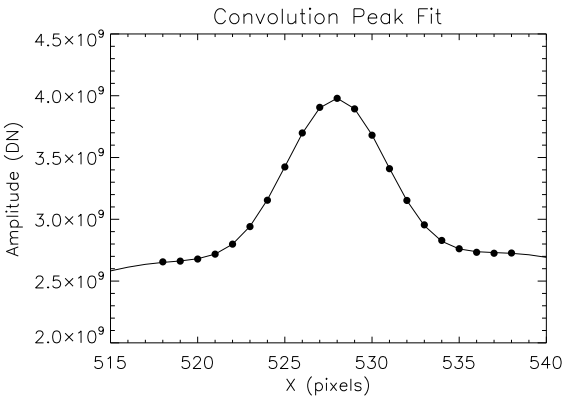

Figure 9. The peak of the convolution matrix overplotted with solid points representing the calculated gaussian fit to the data. Using this method the X centroid of the point of best correlation between a given spectra and the reference spectra is determined to fractional pixel values.

6 Results

Using our neon calibration fit we convert the relative shifts in pixels to relative shifts in units of wavelength. The shift as a function of observation time, extracted from the FITS header, is given in Figure 10:

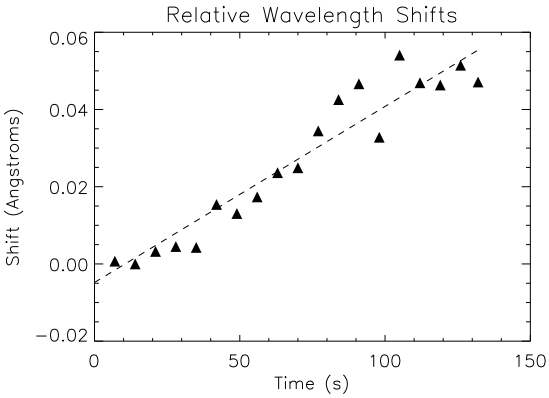

Figure 10. The relative shift of each solar spectrum plotted in units of Angstroms as a function of the time of observation. A clear linear trend exists, as predicted by a constant velocity gradient, with potentially higher order error present.

We expect the points to fall on a linear fit, since the velocity gradient across any chord of the solar disk should be constant. Although there is a clear linear trend, there also appears to be a cubic term. This could be due to the lower SNR achieved near the limbs of the Sun, increased sus-

ceptibility from scattered light, and/or errors in timing resolution during data acquisition. A linear best fit through these points yields a slope of $0.000456 \pm .000031$ Angstroms/sec, where the fractional uncertainty is $\simeq 14.4\%$. If we can calculate the total time necessary to track over the solar disk, the total shift in Angstroms can be obtained.

In order to calculate the time elapsed between when the leading and trailing edges of the sun along the apparent equator pass through the same point on the sky, we obtain the angular diameter of the Sun from the same solar ephemeris[11] as before. On November 29, the angular diameter of the Sun was 1945.7 arcsec. The crossing time t is then given by Equation 17:

$$t = \frac{D}{(360^\circ/84600s)\, cos\,(\delta)} \tag{17}$$

Where D and δ are the angular diameter and declination of the Sun, respectively. The declination of the Sun on the $N = 333^{rd}$ day of the year can be obtained from Equation 18 by considering that it must oscillate between $+23.45^\circ$ and -23.45° over the course of 365 days:

$$\delta = -23.45 * cos\left(\frac{2\pi}{365}\,(N+10)\right) \tag{18}$$

This yields a declination of -21.79° for November 29, 2006, and from Equation 17 we determine a theoretical crossing time at the equator of 139.7 seconds. Multiplying our slope of 0.000456 Angstroms/sec by 139.7 seconds we arrive at a total shift, from edge to edge, of 0.0637 ± 0.0092 Angstroms. Here error would arise due to uncertainty in the timing resolution of our FITS headers. The camera exposure operation takes approximately 6.7 seconds at our 30x1056 readout size. As a result, we would incur a possible underestimation of our actual time over the Sun of up to twice that time, or 13.4 seconds. However, since we are using a theoretical crossing time instead of one derived from the observation session we avoid this issue. Using Equation 1 this equates to a total change in velocity of 3.016 ± 0.43 km/s - or an observed rotational velocity of 1.508 ± 0.21 km/s.

Now, under the geometrical considerations of Section 2.4, with a position angle of 16.9° and a heliocentric latitude of 1.2°, we introduce a correction factor such that $v_{rot} = 1.045 v_{obs}$. Uncertainty in these angles are not given, and so are not considered here. As a result, our final rotational velocity of the solar surface at the equator is 1.576 ± 0.22 km/s.

Finally, we use Equation 2 with a solar equatorial period of 24.66 days[12] to calculate 534,600 $\pm$ 73,760 km for the radius of the Sun. Uncertainty here is large. Due to propagation of error, we have incurred a fractional uncertainty of greater than 10% from the slope fit of the individual shifts alone. The actual radius of the Sun is 695,500 km, a 23.1% error from our calculated radius. However, beyond our upper error bound we are only in error $\simeq 8\%$. This under-estimation of the radius results from an under-estimation of the rotational velocity, which could occur for several reasons.

Due to our collection procedure, we were not guaranteed to capture the solar spectrum at the exact edges of the solar disk. This could result in a lack of information, or more precisely SNR, where it is most needed. Successfully extracting shifts for the extreme edges of the Sun would in all probability contribute to a steeper slope fit on Figure 10, which would increase our radius estimation. This could be implemented by using a guided telescope, and manually slewing over the solar disk. We could then obtain an arbitrarily high number of spectra samples, however several simplying assumptions, such as Equation 17, would no longer hold. Additionally, if our observation chord across the solar disk did not cross through the true equator we could also incur an under-estimation for the total wavelength shift from edge to edge.

7 Conclusion

Considering the limitations of the equipment, however, our estimate of the radius of the Sun represents an extremely difficult measurement. The error, in the Angstroms per second shift rate for our observation, indicates that we have successfully measured fractional pixel shifts of absorption lines on our CCD to a physical precision of greater than 0.26μm. We have effectively increased the resolution of our spectrometer by measuring multiple spectral features at a high signal-to-noise ratio. The combination allows for a measurement of the radius of the Sun with a relatively inexpensive spectrometer. Using scientific instruments with an even greater intrinsic spectral resolution, and the same techniques explored in this paper, we can make extremely accurate

Doppler shift measurements. Velocity resolution on the order of meters per second is achievable, and offers the prospect of detecting orbiting planets around distant stars. With emerging technology this technique will allow the detection of Earth-mass terrestial planets - a quest which is perhaps one of the most exciting in observational astronomy.

References

[1]CRC Handbook of Chemistry and Physics, 61st ed. Florida: CRC Press.

[2]Graham: "Spectroscopic Measurement of Solar Rotation Using the Doppler Shift", eq 13.

[3]Graham: "Spectroscopic Measurement of Solar Rotation Using the Doppler Shift", eq 17.

[4]Graham: "Spectroscopic Measurement of Solar Rotation Using the Doppler Shift", eq 22.

[5]http://sunearth.gsfc.nasa.gov/eclipse/TYPE/sunkey.html

[6]http://physics.nist.gov/PhysicsRefData/Handbook/

[7]http://www.noao.edu/kpno/specatlas/henear/henear.html

[8]An optimal window for a time-sequence of data needed to maximize signal and minimize spectral artifacts would be a discrete prolate spheroidal windowing function.

[9]Graham: "Spectroscopic Measurement of Solar Rotation using the Doppler Shift", eq9.

[10]Bracewell: "The Fourier Transform and Its Applications" p25.

[11]http://sunearth.gsfc.nasa.gov/eclipse/TYPE/sunkey.html

[12]Handbook of Chemistry and Physics. 61st ed. Florida: CRC Press.